

Evidence for ice flow prior to trough formation in the martian north polar layered deposits

Dale P. Winebrenner^{a,b,*}, Michelle R. Koutnik^b, Edwin D. Waddington^b, Asmin V. Pathare^{c,d},
Bruce C. Murray^d, Shane Byrne^e, Jonathan L. Bamber^f

^a Applied Physics Laboratory, Box 355640, University of Washington, Seattle, WA 98195, USA

^b Department of Earth and Space Sciences, Box 351310, University of Washington, Seattle, WA 98195, USA

^c Planetary Science Institute, 1700 E. Ft. Lowell, Suite 106, Tucson, AZ 85719, USA

^d Division of Geological and Planetary Sciences, California Institute of Technology, Pasadena, CA 91125, USA

^e Lunar and Planetary Laboratory, The University of Arizona, Tucson, AZ 85721, USA

^f Bristol Glaciology Centre, University of Bristol, Bristol BS8 1SS, UK

Received 27 August 2007; revised 29 October 2007

Available online 12 January 2008

Abstract

The relative importance of surface mass fluxes and ice flow in shaping the north polar layered deposits (NPLD), now or in the past, remains a fundamental and open question. Motivated by observation of an apparent ice divide on Gemina Lingula (also known as Titania Lobe), we propose a two-stage evolution leading to the present-day topography on that lobe of the NPLD. Ice flow approximately balances surface mass fluxes in the first stage, but in the second stage ice flow has minimal influence and topography is modified predominantly by the formation of troughs. We focus here on evidence for the first stage, by testing the fit of topography between troughs to an ice-flow model. We find that independent model fits on distinct flow paths closely match inter-trough topography, uniformly over a broad region on Gemina Lingula, with mutually consistent and physically reasonable fitting parameters. However, our model requires ice to occupy and flow in spaces where troughs currently incise the ice. We therefore infer that the troughs (and the distribution of mass balance that caused them) post-date deposition of the inter-trough material and its modification by flow. Because trough formation has apparently altered inter-trough topography very little, we infer that trough formation must have been rapid in comparison to the (still unknown) time-scale of flow since troughs began to form. We view the evidence for past flow as strong, but we do not think that topographic evidence alone can be conclusive. Observations of englacial stratigraphy using orbital sounding radars will yield conclusive tests of our inferred mechanism for the formation of inter-trough topography.

© 2008 Elsevier Inc. All rights reserved.

Keywords: Mars, polar caps; Geophysics; Ices

1. Introduction

The north polar layered deposits (NPLD) are the largest surface reservoir of martian water ice that actively exchanges with the atmosphere. Their nearly complete lack of impact craters suggests that their surface is geologically young, or has been recently and extensively modified (Herkenhoff and Plaut, 2000). Alternating bright and dark layers can be seen along the walls of arcuate troughs that cut through the NPLD. This layered

structure likely reflects deposition during orbitally-driven climate changes (Touma and Wisdom, 1993; Laskar et al., 2002; Levrard et al., 2007), which may have been modified subsequently, both within and between troughs. Hence, understanding the mechanics and evolution of the NPLD is necessary to decipher any evolution of martian climate recorded in the layers.

It is generally assumed that topography and layering of the NPLD are governed by two processes: ice deposition and loss at the surface (mass balance), and ice flow. However, the relative importance of these processes in shaping the NPLD, now or in the past, remains a fundamental and open question.

* Corresponding author.
E-mail address: dpw@apl.washington.edu (D.P. Winebrenner).

To set a framework in which to discuss this question, we introduce two characteristic time scales. The first is the time required to build up an ice sheet through accumulation alone at some characteristic accumulation rate, or equivalently, to remove it by ablation alone at some characteristic ablation rate. The second is the time for material to move a characteristic distance, such as the length of the ice mass, by flow at some characteristic speed. The ratio of these two characteristic times gives a nondimensional number F , which we call a *flow number*. In Appendix A, we use conservation laws for mass and momentum together with a temperature-dependent constitutive relation for ice to derive expressions for both of these characteristic time scales and for F in terms of characteristic values of accumulation rate, temperature, and ice-mass dimensions. When $F \ll 1$, mass exchange with the atmosphere alone controls surface topography, and the ice mass is stagnant. When F is of order unity, both surface mass exchange and ice flow influence the surface shape, and the ice mass can be in a near-equilibrium state. When $F \gg 1$, ice flow alone controls surface-elevation changes, and surface mass exchanges are negligible. On Earth, surging glaciers (Kamb et al., 1985) fall in this regime. However, most terrestrial ice masses are in a near-equilibrium regime with F of order unity.

Some researchers have modeled the NPLD as a near-equilibrium regime with F of order unity. Budd et al. (1986) first modeled the NPLD as a large-scale, steady-state flow system. Zuber et al. (1998) and Zwally et al. (2000) interpreted Mars Orbiter Laser Altimeter (MOLA) data from the NPLD as supporting that view. Fisher (1993, 2000) developed a model to explain more detailed NPLD topography by incorporating flow with an alternating pattern of accumulation and sublimation resulting from local radiative effects of troughs (i.e., “accublation”). Fisher et al. (2002) found evidence in the directionality of NPLD surface texture for flow in the directions expected from large-scale topography. Modeling by Hvidberg (2003) and by Pathare and Paige (2005) also supports a role for ice flow in shaping the NPLD, especially near troughs. Nye (2000) even considered martian ice caps shaped entirely by flow in the absence of surface mass fluxes ($F \gg 1$).

However, modeled ice flow speeds on Mars are generally very slow, even during high obliquity and during NPLD formation, so surface mass balance can easily dominate flow in producing the modeled shape (Greve et al., 2004; Greve and Mahajan, 2005). Ivanov and Muhleman (2000), in fact, argue that the observed NPLD topography can be explained by sublimation alone. Fishbaugh and Hvidberg (2006) conclude that internal layers in the upper portion of the NPLD show no evidence of flow, i.e., that the NPLD are currently in a stagnant regime with $F \ll 1$.

Thus there is presently no consensus on the roles of surface mass fluxes and ice flow in shaping the NPLD as a whole. This suggests investigation of new alternatives, including a search for parts of the NPLD on which effects of relatively recent processes may be most evident. Our investigation is motivated by an examination of MOLA data shaded to emphasize regions that are simultaneously high in elevation and low in slope

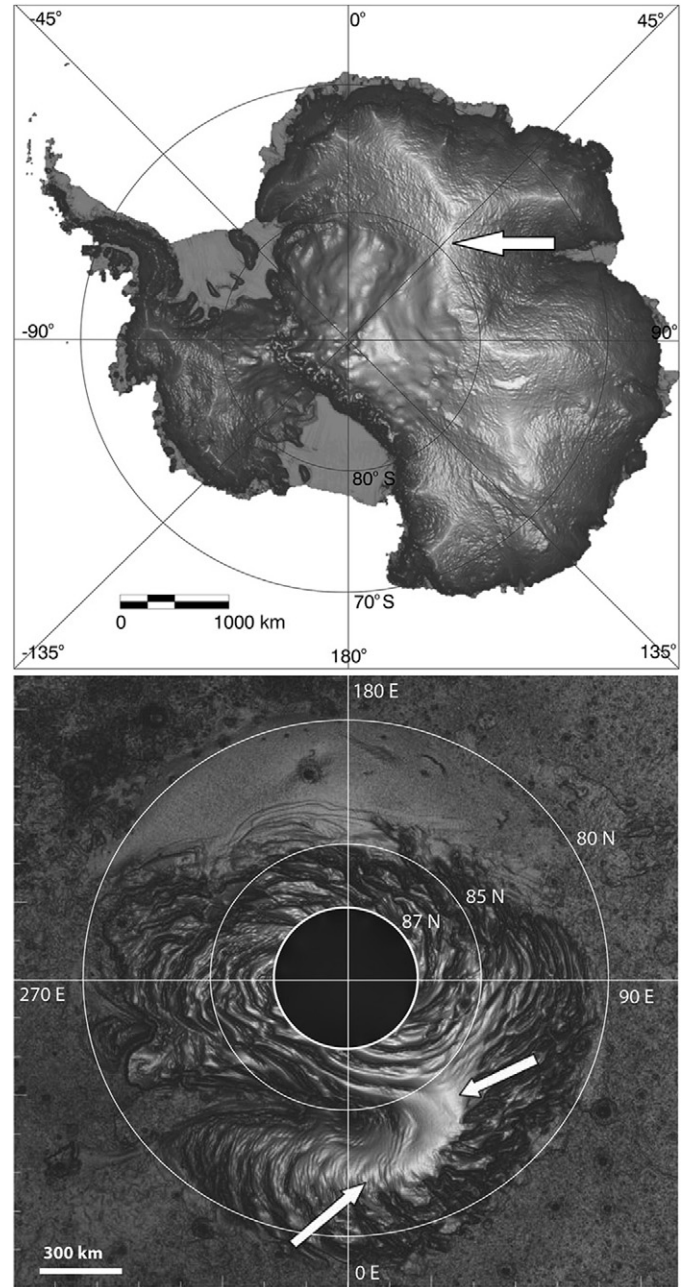


Fig. 1. (a) Digital elevation data for Antarctica, shaded to highlight areas that are both high in elevation and low in slope (Bamber, 2004). The arrow indicates one ice divide among several visible. (b) Digital elevation data from the MOLA laser altimeter for the NPLD. Here we use the 512-point-per-degree DEM, which does not include data for locations poleward of 87° N (Smith et al., 2003). Shading in this presentation is identical to that in (a). Arrows indicate a contiguous topographic feature that appears similar to ice divides on Earth.

(Bamber, 2004; Ekholm et al., 1998). On Earth, such shading effectively highlights ice divides, which are boundaries separating regions of flow in different directions. The locations, or absence, of ice divides are key features on any ice cap. Surface slopes on terrestrial ice divides tend to be low and slowly varying, and divides tend to be lines with low curvature in map view. Fig. 1 shows digital elevation models (DEMs) for

Antarctica and the NPLD, shaded identically and as described above. We focus here on the lobe of the NPLD that bounds Chasma Boreale to the south and east, which has recently been named Gemina Lingula by the International Astronomical Union. Here we refer to this feature as Titania Lobe (Pathare and Paige, 2005). A ridge running along the lobe resembles ice divides on both Antarctica and Greenland (Ekholm et al., 1998; Bamber, 2004).

While resemblance does not establish analogous ice dynamics on Earth and Mars, it does suggest quantitative tests based on topography. The relative lack of troughs cutting the candidate divide suggests to us that present-day topography between troughs may preserve evidence of ice flow in a previous era. The layering observed along PLD trough walls also clearly indicates that troughs formed after the inter-trough topography by cutting into pre-existing ice (Cutts, 1973; Howard et al., 1982; Thomas et al., 1992).

We therefore consider a new approach to the question of whether ice flow has influenced NPLD structure, at least on Titania Lobe. Rather than trying to explain topography on this lobe with one set of processes acting at all times (with or without flow), we propose a two-stage evolution leading to the present-day NPLD. Ice flow and surface mass exchanges were approximately balanced in the first stage (i.e., $F \sim 1$), but a second stage followed and continues up to the present in which $F \ll 1$; ice flow has had minimal influence in this second stage and topography has been modified predominately by the formation of troughs.

We begin testing this scenario by ignoring the troughs (for now), and testing current topography on Titania Lobe, between the troughs (cf. Section 2.1, Fig. 4) for evidence that the first stage of evolution actually occurred. Specifically, we solve an ice-flow inverse problem by fitting an ice-flow model to observations, thus estimating mass balance and flow parameters within the model scenario. (This stands in contrast to solution of a forward problem, in which parameters and forcing are prescribed and the ice-flow model predicts observables.) Experience with analogous inverse problems on terrestrial ice caps (Waddington et al., 2007; see also Section 4) indicates that if no flow has occurred, solutions of the inverse problem will fit observed topography poorly, or solutions on distinct parts of the topography will yield inconsistent and unphysical parameter inferences. Solutions that agree with the actual topography, using mutually consistent and physically reasonable parameters, would be evidence that a balance between mass fluxes and flow did in fact govern formation of the topography between troughs.

We find that independent model fits on distinct flow paths in fact closely match inter-trough topography, uniformly over a broad region on Titania Lobe. The parameters inferred from distinct fits are mutually consistent across the region. The previous ice extent inferred from fitted parameters closely tracks the present margin of the lobe, except in part of Chasma Boreale (where it diverges plausibly). The inferred pattern of mass balance is plausible, and the inferred ice-flow law coincides with that commonly found in flowing ice masses on Earth.

While we do not think that topographic evidence alone can be conclusive, we interpret our results as strong evidence for the occurrence of the first stage in our scenario.

In that first stage, however, ice would have occupied and flowed in spaces where troughs currently incise Titania Lobe. We therefore infer that the troughs post-date deposition of the inter-trough material and its modification by flow—i.e., the consistency of fits is evidence that the second stage of our scenario also occurred (though we do not attempt to model that second stage here). Because our assumed spatial distribution of mass balance differs strongly from that necessary to explain troughs, we also infer a fundamental change in the mass-balance distribution on Titania Lobe. Finally, because trough formation has apparently altered inter-trough topography very little, we infer that trough formation must have been rapid in comparison to the (still unknown) time-scale of flow since troughs began to form.

This remainder of this paper is organized as follows: Because the particular methods employed here are not explicit in literature on terrestrial ice masses, we present our methods in Section 2, with details in Appendix A. Section 3 presents numerical results of our analysis on individual topographic profiles as well as the statistics of parameters inferred from 40 profiles covering a broad swath on Titania Lobe. We discuss interpretation of the numerical results in Section 4. Section 5 presents conclusions and our views on further work, particularly with regard to radar-observed stratigraphy within the NPLD which could conclusively test our inferences, and could yield more detailed information on past and present flow dynamics and mass balance.

2. Methods

Throughout this work, we use the 512-point-per-degree (ppd), polar-stereographic projection of the MOLA DEM of the NPLD, which is composed of square pixels measuring approximately 115.09 m on a side (Smith et al., 2003).

The geometrical specification of our problem requires an assumption for the basal topography beneath Titania Lobe. We assume that topography is constant in elevation at -5100 m relative to the martian geoid, consistent with the exceptional flatness of surrounding topography and with a recent radar observation showing no evidence for lithospheric deflection beneath the NPLD near Titania Lobe (Picardi et al., 2005).

Our methods then divide naturally into two parts: (1) operations on the MOLA DEM to specify surface elevation data for use in an ice-flow inverse problem; and (2) specification and solution of the inverse problem.

2.1. Delineation of inter-trough topography, candidate flow lines and flow bands

To compare MOLA data with an ice-flow model, we must first delineate objectively topography that would preserve information about flow. According to our hypothesis, this is topography between troughs. Topography on Titania Lobe outside of troughs generally has small slopes compared to slopes on

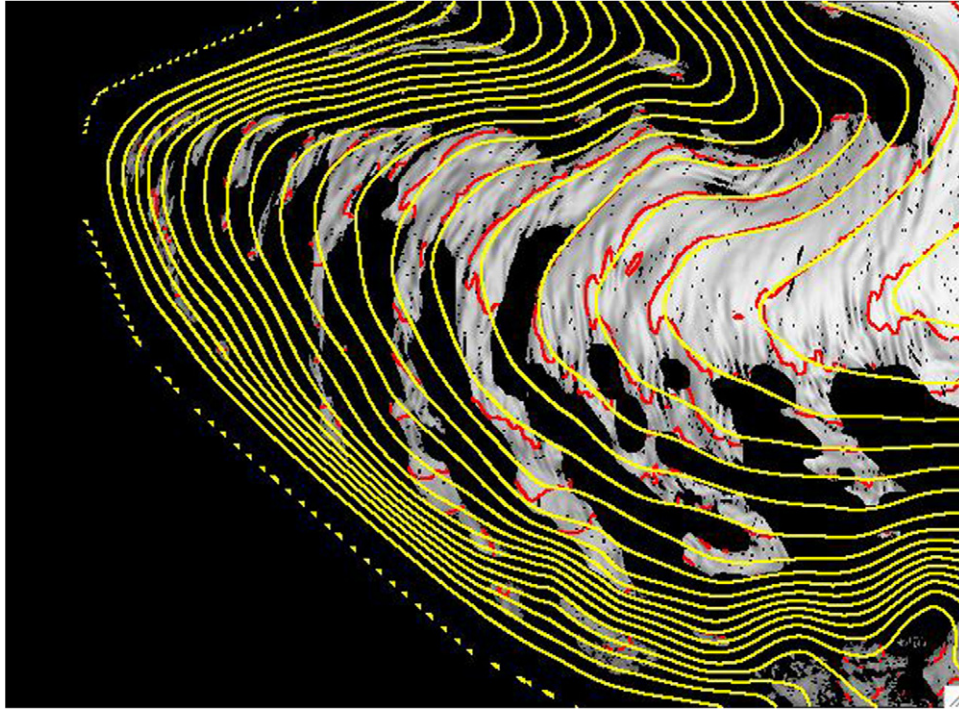


Fig. 2. Elevation contours with 300 m spacing on the MOLA DEM (red) and on the interpolated, smoothed surface derived from inter-trough topography (yellow). The underlying shaded-relief is the MOLA DEM (with shading identical to that in Fig. 1b) restricted to inter-trough topography as delineated by our procedure. Gradient paths orthogonal to the yellow contours thus coincide with prospective ice flow paths on inter-trough topography, and they traverse troughs on paths that ice flow would have taken prior to trough formation (i.e., at a previous time when the now-empty troughs were filled with ice).

trough walls. Empirically, we find that topography with elevation gradients less than 0.015 rad (0.86°) in magnitude coincides with inter-trough topography as determined by inspection, except in small areas at the bottoms of troughs where the dominant slopes change sign. After removal of such areas, the remaining low-slope DEM pixels constitute our estimate of inter-trough topography. (For quantitative details see Appendix A.)

Next, we identify prospective flow lines as elevation gradients on a smooth surface that we derive from inter-trough topography by bridging the troughs across their tops and smoothing the result. Elevation contours on the interpolated, smoothed surface closely match those of the original MOLA data for locations on the inter-trough topography (Fig. 2). Gradient lines on the smoothed surface therefore coincide with those derived purely from MOLA data on inter-trough topography, but span the troughs on paths that ice flow would take, were the troughs filled with ice.

Fig. 3 shows 51 gradient paths on the interpolated, smoothed surface overlain on the MOLA DEM. The paths are chosen to cross the -4900 m elevation contour (200 m above Vastitas Borealis surrounding Titania Lobe), at roughly constant spacings of 12 km. Of the 51 paths, 40 climb toward the divide shown in Fig. 1b with smoothly, monotonically decreasing separations, analogous to similar paths on terrestrial ice sheets. We refer to these paths as ‘regular.’ They cover a broad swath of the lobe which spans approximately 400 km (cf. Fig. 1b), starting on the western (chasma) side of the tip, extending over much of the southern side of the lobe, and including all of the terrain where

inter-trough topography spans a wide range of elevations. Fig. 4 illustrates MOLA elevations and inter-trough topography along a typical gradient path on the south side of the lobe.

The remaining 11 paths are the eastern-most paths on the southern side of the lobe (cf. Fig. 1b), where inter-trough topography extends down only to about -3900 m elevation on the MOLA datum. Separations between these flow paths widen and narrow irregularly as they climb toward the divide, and are particularly irregular at locations of troughs in the actual topography. We refer to these paths as ‘irregular.’

Because prospective flow line separations vary, it is useful for ice flow modeling to consider flow bands centered on each line, i.e., curvilinear slices of topography defined such that flow across boundaries between bands would be negligible compared to that in the direction along each line (Waddington et al., 2007). We derive flow bands for each flow line in Fig. 3 using 2 additional gradient-paths on the interpolated, smoothed inter-trough topography which are spaced approximately 3 km on either side of the flow line at the -4900 m elevation contour (for details see Appendix A).

The data to be used for solution of our flow inverse problem are thus: (1) elevations from the MOLA DEM along the prospective flow lines where they traverse inter-trough topography; and (2) corresponding flow-band widths along the lines. Note that elevations on the interpolated, smoothed surface define candidate flow lines, and thus the selection of MOLA data, but it is the MOLA elevations, *not* elevations on the smoothed, interpolated surface, that are compared with the ice-flow model.

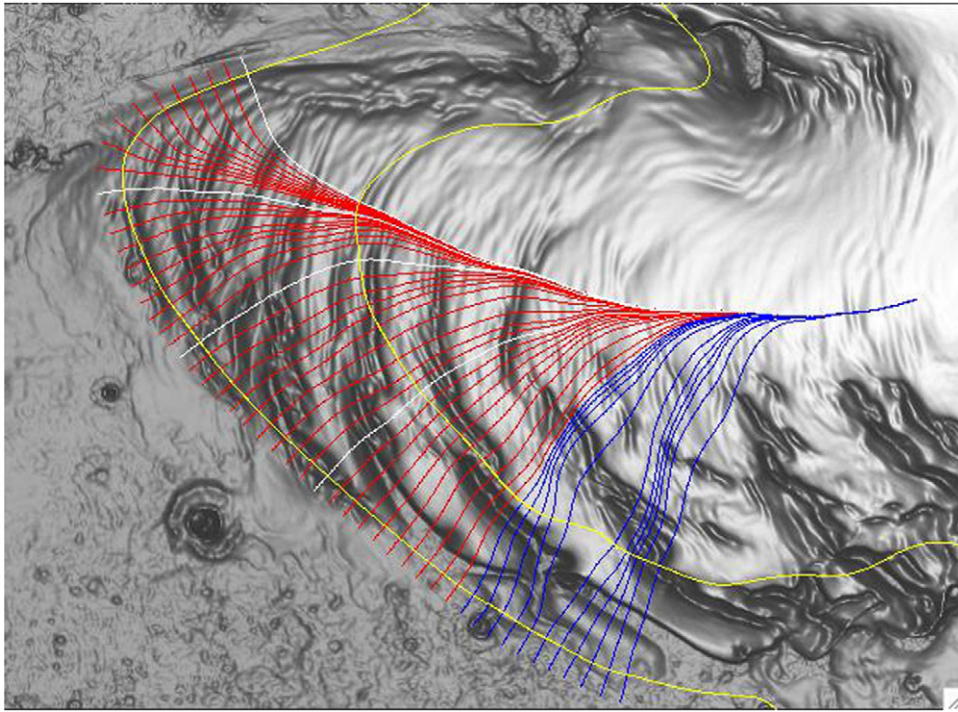


Fig. 3. Paths along elevation gradients on the smoothed, interpolated surface derived from inter-trough topography, superimposed on the MOLA DEM of Titania Lobe. Two elevation contours are also shown, the lower at -4900 m (200 m above the part of Vastitas Borealis surrounding Titania Lobe) and the higher at -3900 m. Eleven of the paths (shown in blue) are ‘irregular,’ as defined in the text. The remaining 40 (shown in red and white) are ‘regular’; these paths constitute our estimates of ice flow lines, if and when ice actually did flow on Titania Lobe. (We number the regular, paths starting with the westernmost path on the side of the tip in Chasma Boreale, for reference. Paths 1, 11, 21, and 31 are shown in white for reference.) We use the pixel locations that constitute regular paths to select elevation data from the MOLA DEM for comparison with an ice-flow model. Elevations from the smoothed, interpolated surface are not compared with the model.

2.2. Specification and solution of an ice-flow inverse problem

Next, we specify a model for the topography of a flowing ice mass with a parameterized distribution of surface mass fluxes. Large-scale topography is more sensitive to ice dynamics than to the spatial distribution of surface mass balance, and thus by itself can yield information only on the gross pattern of balance (Paterson, 1994). Even the gross mass-flux pattern on the surface of Titania Lobe is highly uncertain (observations are lacking and mechanisms responsible for the balance are poorly known). However, the overall shape of inter-trough topography—decreasing slope with increasing elevation—and the position of the apparent ice divide suggest to us a pattern of accumulation at higher elevations and ablation (via sublimation) at lower elevations at the time when inter-trough topography formed. Such a pattern would be somewhat similar to that proposed by Fisher (1993), who argued that the presence of a second spreading center in Titania Lobe distinct from the main cap could explain the overall spiral pattern of troughs on the NPLD.

Thus, without speculating on what physics would produce such an Earth-like pattern on Mars, we assume a steady-state surface mass balance rate (units ice volume $\text{area}^{-1} \text{time}^{-1}$) with uniform (spatially constant) accumulation along a given flow line, starting at the ice divide and extending downhill to an equilibrium-line location, which is to be determined by the model fit. Mass balance at the equilibrium line changes discontinuously from accumulation to ablation. We then assume

a uniform ablation rate between the equilibrium line location and the terminus of the flow line (see Fig. 4b). The assumption of a steady state implies that the equilibrium-line location depends only on the geometry of the flow band and on the ratio of accumulation and ablation rates, rather than on their absolute values.

Maintenance of steady-state topography requires ice to flow from regions of accumulation to regions of ablation. (A quantitative version of this requirement is given in Appendix A.) We assume that the ice in Titania Lobe is, and has always been, frozen to its bed, so that there is no mass flux across its lower boundary. Then at each point, P , along the flow line, the mass flux due to flow through a vertical cross-section of the flow band must balance the surface mass flux into the band integrated from P up to the ice divide (where the flow-band width, and therefore surface mass flux into the band, decreases to zero). We link this kinematic balance to the surface slope at P by assuming that the driving stress is determined solely by the surface slope and ice thickness at P , and that there is no sliding at the bed (consistent with the frozen-bed assumption). We express the mass flux through the flow-band cross section in terms of a depth-averaged velocity. The latter can be derived from the assumptions on driving stress and bed elevations, together with a flow law to relate strain rate to stress in the ice. We assume a power-law form for the flow law, with exponent n (Glen, 1955; Goldsby and Kohlstedt, 2001), which we take as a parameter. We take the temperature-dependent factor in the flow law, and thus temperature, to be constant over depth and over the flow

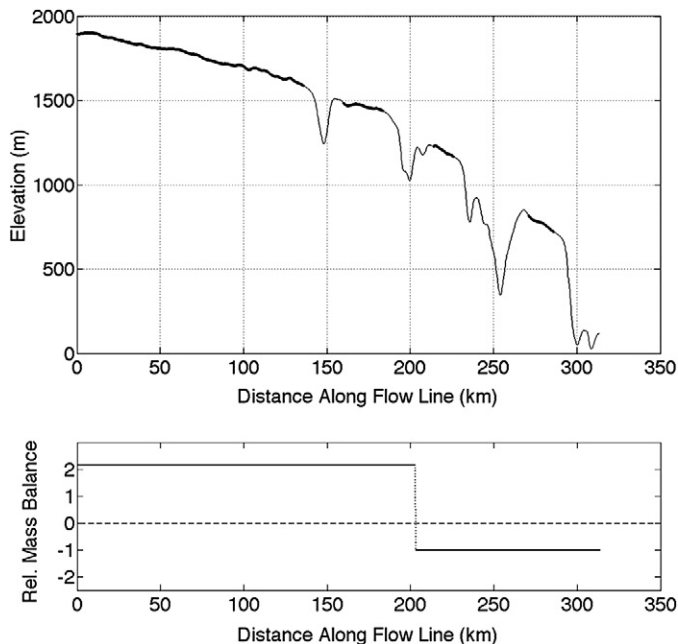


Fig. 4. (a) MOLA elevation data along regular gradient path 29, on the south side of Titania Lobe, with elevations given as meters above -5100 m. Elevations located on inter-trough topography, as shown in Fig. 2, are denoted by heavy black lines. (b) A generic example of the spatial pattern of surface mass balance rate (units ice volume $\text{area}^{-1} \text{time}^{-1}$) along the gradient path, as assumed in our model (cf. Section 2.2). The mass balance is positive (onto the ice mass) and uniform (spatially constant) from the ice divide to an equilibrium-line location, which is to be determined by model fitting. Mass balance at the equilibrium line changes discontinuously from positive (accumulation) to negative (ablation due to sublimation). The ablation rate is then uniform between the equilibrium-line location and the terminus of the flow line. Our model fits determine only relative magnitudes of accumulation and ablation (cf. Section 2.2 and Appendix A)—hence rates in this plot are relative rather than absolute, and would be multiplied by the ablation rate (were it known) to obtain absolute rates.

lines. Integration of surface slope along the flow line then yields the surface-elevation profile. We give a mathematical formulation of this model in Appendix A. Our model is, however, only a slight generalization of that given by Paterson (1972), and it reduces to that model for a flow band of uniform width.

As in Paterson’s model, the equilibrium-line position sets the spatial pattern of ice velocities, but not their absolute magnitudes—the steady-state condition equally allows slow flow with small surface fluxes, or faster flow with larger fluxes. The model fits shown below therefore provide no information on rates at the time that inter-trough topography formed. Our model does, however, couple ice temperature near the bed (where most strain occurs) to flow speeds and absolute mass flux rates. Thus a combination of this work with englacial temperature modeling (e.g., through obliquity cycles) will provide estimates of absolute rates and characteristic time-scales for the formation of inter-trough topography by flow. We discuss such future work in the final section of this paper, but our aim here is first to address the question of whether inter-trough topography in fact preserves evidence of flow.

The final element of our method is a particular algorithm to solve the inverse problem. Note that all topographies that can be

generated by our model vary slowly on the scale of the ice thickness. We seek to interpret the large-scale topography of Titania Lobe, rather than the fine-scale topography observed between troughs (which is presumably due to more complex patterns of mass balance, or perhaps bed topography, than can be diagnosed from surface topography alone). The smoothness of all model topographies relative to the data, and the small number of model parameters relative to independent data points, prevents over-fitting; thus constraining fits (using, for example, Lagrange multipliers) proves to be unnecessary. Moreover, for this initial work, we seek a very straightforward inverse method, even at the cost of quantitative information on uncertainties in our fitted parameters (i.e., resolving power).

We therefore fit our model to inter-trough topography simply by minimizing the mismatch between model and data, in the least-squares sense, as we vary 4 model parameters: (1) the ice thickness, H , at the highest point on the flow line, i.e., where the flow band width decreases to zero on the ice divide; (2) the extent, L , of the model topography along the flow line; (3) the position of the equilibrium line along the flow line; and (4) the flow-law exponent, n . We fit the model on each flow line independently of fits along any other flow lines, so each fit yields independent parameter estimates. Consistency between parameter estimates from distinct flow lines indicates consistency in the physics contained in the model and the topography at different locations on Titania Lobe.

3. Results

On 39 of the 40 regular paths (cf. Section 2.1), the ice-flow model fits the observed inter-trough topography to within a root-mean-square (RMS) mismatch of 10–26 m, which is 1–2% of the range of inter-trough topography elevations along the flow lines. The remaining path, on which the RMS mismatch is 32 m, is the path most closely neighboring the irregular paths (path 40). We show below that these fitted model topographies, i.e., fits, closely track both the elevations and slopes of inter-trough topography over the entire region of regular paths. The question is therefore whether the inferred model parameters are consistent and physically reasonable.

Because topography is more sensitive to flow dynamics than to the spatial pattern of mass balance, consider first consistency with respect to the ice flow-law exponent, n . Fig. 5 shows histograms of the RMS mismatches for several values of n . The value $n = 1$ corresponds to linear, viscous (Newtonian) flow, such as may occur in ice at very low strain rates (e.g., Pettit and Waddington, 2003). The value $n = 1.8$ occurs for ice with grain sizes on the order of microns and under cold conditions (Goldsby and Kohlstedt, 2001), and thus might be expected to apply on Mars (Pathare and Paige, 2005). Values of $n = 3$ to 4 are characteristic of ice flow on Earth at relatively high strain rates, with grain sizes on the order of millimeters and basal temperatures greater than about -12 °C, while $n = 6$ approximates the flow law for perfectly plastic material (Paterson, 1994).

Perhaps surprisingly, fits with the smaller exponents yield considerably poorer fits than those obtained with $n = 3$ and $n = 4$ —the distributions of best-fit RMS mismatches for $n =$

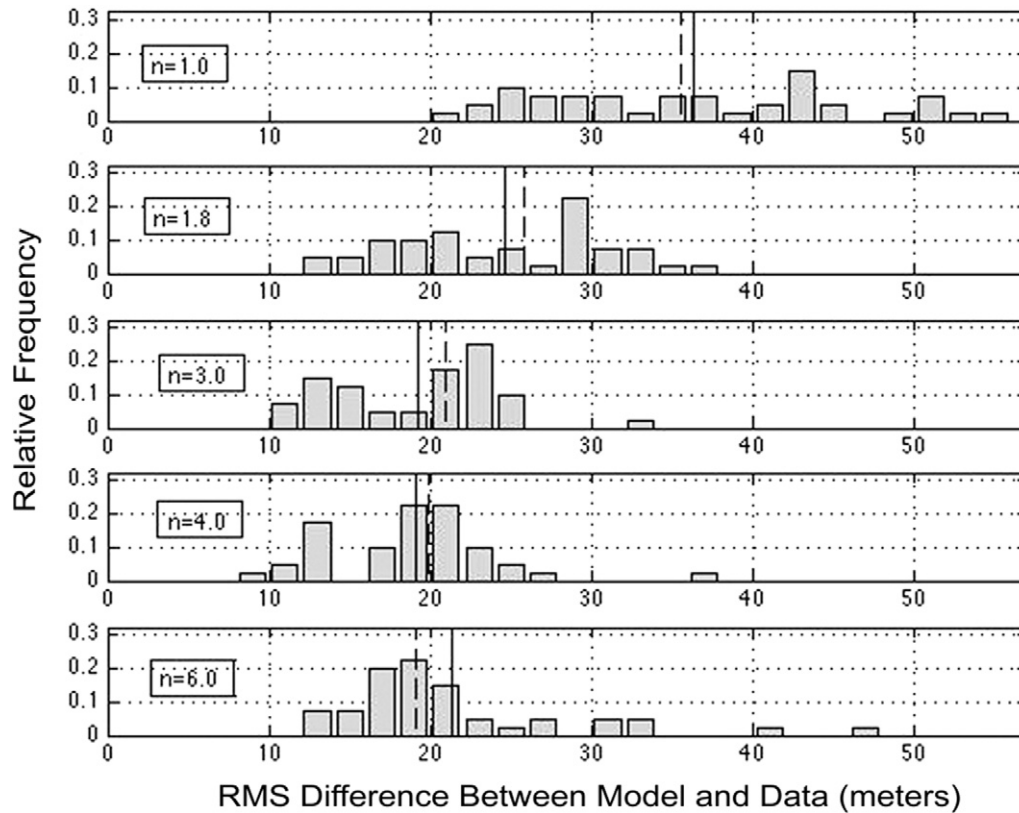


Fig. 5. Histograms of RMS mismatches between the MOLA DEM on inter-trough topography and best-fit model elevations, on the 40 flow lines shown in red in Fig. 3, for 5 values of the flow-law exponent, n . Relative frequencies sum to 1, and the dashed and solid lines indicate the median and mean values, respectively, for each value of n . RMS mismatches are smallest, and the distributions most compact, for $n = 3$ and $n = 4$, with little to distinguish distributions for those values of n . Larger values of n yield the lowest values of RMS mismatch in some cases, but are generally not optimal and yield larger numbers of large RMS mismatches than do $n = 3$ and $n = 4$.

3–4 have the smallest means and nearly the smallest medians. They include the smallest mismatches observed for any values of n , and they include the fewest large mismatches in any of the distributions. Fits with $n = 6$ yield the lowest median RMS mismatch, but also yield more large mismatches than those with $n = 3$ –4. We show below that those profiles that are fit well with $n = 6$ may yield some additional insight. However, flow-law exponents of 3–4 clearly yield excellent fits to all of the 40 regular profiles and are the best values overall for fitting that set.

Inspection of individual fits shows that the fits are accurate not only statistically, but also point by point along each profile. The flow-line elevations in Fig. 6a are from the southern side of Titania Lobe, where inter-trough topography occurs over a broad range of elevations. The flow line is one of the regular paths, and the fit is representative of those from the southern side of the lobe. In this case, the best-fit profile with $n = 3$ fits the data slightly better than that with $n = 4$ (RMS mismatches of 10.5 m vs 12.7 m), but both fits follow the actual shape of inter-trough topography very closely. Estimates of equilibrium-line positions differ somewhat between values of n , but the difference is similar to the widths of the minima in RMS mismatches between model and data (Fig. 6b).

By contrast, our model fails to fit accurately the elevations along paths on parts of Titania Lobe with (apparently) little remaining inter-trough topography, as shown in Fig. 7. The flow line in Fig. 7 is one of the 11 irregular lines, along which most

inter-trough topography is confined to high elevations. RMS mismatches for this and neighboring flow lines exceed 44 m (and are not included in the histograms in Fig. 5). Moreover, modeled and observed topographies differ even qualitatively (except at the highest elevations). Thus consistency between results on various paths is not somehow inherent in our model, but rather indicates a physically consistent explanation in those locations where it occurs.

Fig. 8 shows fits from a spatially extensive sample from the 40 regular profiles in Fig. 3, spanning the area from the tip of Titania Lobe around to the region of irregular profiles. Fits in all of these cases, as well as that shown in Fig. 10 and the 30 remaining regular cases not plotted here, are much more similar to those in Fig. 6 than to those in Fig. 7—fits with flow-law exponents of 3 and 4 closely track inter-trough topography from 400 m to 1900 m above Vastitas Borealis (i.e., from -4700 to -3200 m).

There is also consistency between the other model parameters inferred from individual flow lines. Fig. 9 shows for all 40 profiles the inferred termini of the flow lines, i.e., the inferred extent of the ice cap at the time of flow; results for fits with $n = 3$ and $n = 4$ are shown in red and white, respectively. Estimates of terminus positions are tightly determined by the fits and differ little for the two flow law exponents. They are mutually consistent between independent flow lines, and moreover they track the present-day extent of Titania Lobe closely

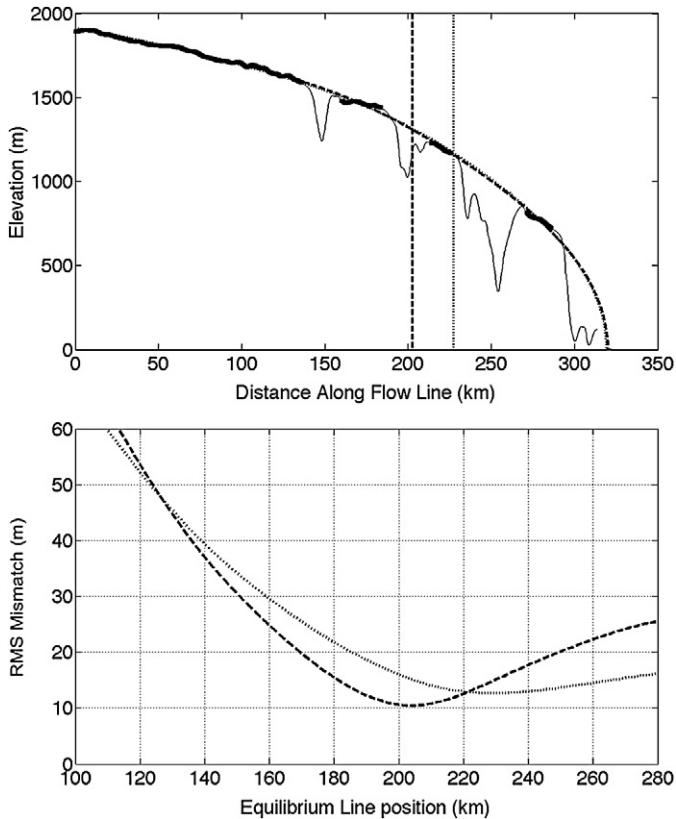


Fig. 6. (a) Representative data and model fits from path 29, on the southern side of Titania Lingula away from the tip. MOLA data along the flow line are shown by the thin black line, with elevations given as meters above -5100 m. Inter-trough topography is shown by the thick black line. (The data and flow line for this figure are identical to those in Fig. 4.) The dashed curve is the result of minimizing the RMS mismatch between inter-trough elevations and the model over all values of H , L , and equilibrium position, R , while holding the flow-law exponent, n equal to 3. The estimated position of the equilibrium line is marked by the dashed vertical line. The minimized RMS mismatch is 10.5 m. Dotted lines show the corresponding fit and estimate of equilibrium line position with $n = 4$, for which the RMS mismatch is 12.7 m. The fit with $n = 4$ is difficult to distinguish from that with $n = 3$ at this scale. (b) Plots of RMS mismatches between inter-trough elevations and fits as position of the equilibrium line is allowed to vary (and best-fit values H and L are chosen separately for each equilibrium line position). Mismatches for fixed $n = 3$ and $n = 4$ are plotted as dashed and dotted lines, respectively.

(though flow lines terminating in Chasma Boreale suggest an earlier extension of the ice into that feature). Our procedure infers the ice thickness at the divide (i.e., at the head of the flow band) as well. The inferences are strongly constrained by our assumption for basal topography and the MOLA-observed elevations on the divide. They therefore closely and consistently track the divide elevations, though mainly by virtue of their strong constraint by the data.

The fourth and final set of inferred parameters are the positions of equilibrium lines. The solution of our inverse problem yields the least resolution for those positions (cf. Figs. 6b and 10b), consistent with the relative insensitivity of topography to mass-balance distributions. Equilibrium-line positions from fits with $n = 3$ (in red) and $n = 4$ (in white) in Fig. 9 display some pseudo-random variability, and fits with the larger exponent yield slightly lower-elevation positions. All of the es-

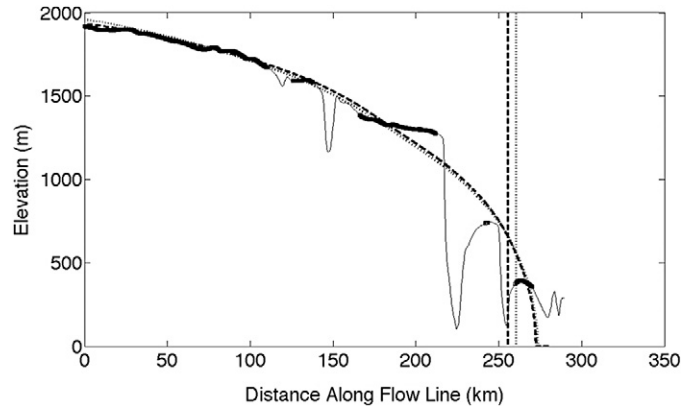


Fig. 7. Data and model fits from one of the flow lines that converge irregularly toward the divide on the southern side of Titania Lingula (cf. Fig. 3—this path is number 42 if we extend the numbering of regular paths into the irregular paths). Fits are for flow law exponents $n = 3$ (dashed, RMS mismatch between model and data of 44.5 m) and $n = 4$ (dotted, 51.6 m RMS mismatch). The fits here are not only quantitatively less accurate than those in Fig. 6, but also differ qualitatively in shape from the data.

timates, however, lie between -3900 and -4300 m, generally trending from higher in the east to lower in the west. Such a trend could plausibly result from atmospheric (or perhaps radiation-driven) processes, and certainly stands in contrast to uncorrelated variations over a large region on the lobe. The inferred equilibrium-line positions therefore also appear to be consistent, within the apparent limits on our resolving power for that variable.

Thus, the high-fidelity model fits to inter-trough topography, on 40 independent profiles covering a broad area on Titania Lobe, are obtained with mutually consistent values for all inferred parameters. This is our primary result.

There may, in addition, be some insight available from a slight, but systematic, difference in fits on different parts of the lobe. Specifically, the 40 regular flow lines divide into two spatially contiguous groups, distinguished by the behavior of RMS mismatches of fits versus n : (1) a group of 22 lines on the southern side of the lobe, which starts at the boundary with the irregular lines and extends westward toward (but does not reach) the tip of the lobe; and (2) a group of 18 lines, which covers the tip of the lobe on both its northern and southern sides. In the first group, the RMS mismatches of fits attain their global minima for values of $n = 3-4$; RMS mismatches of the best possible fits holding $n = 6$ exceed those with $n = 3-4$ by a few meters up to a maximum of 13 m. Thus fits on the southern side of Titania Lobe clearly favor flow-law exponents in the range 3-4 over all other flow law exponents tested.

Fits in the second group with $n = 3$ to 4 also track inter-trough topography very closely (see Figs. 8 and 10), with RMS mismatches in the range 20-26 m. Fits with $n = 6$ in this group, however, yield model elevations which differ by no more than a few meters, anywhere along the flow line, from those obtained with $n = 3-4$. The minimum RMS mismatches with $n = 6$ are 0-3.5 m lower those for $n = 4$. In fact, minimum RMS mismatches decrease yet further with increasing n , up to at least $n = 7.5$ (the largest value of n that

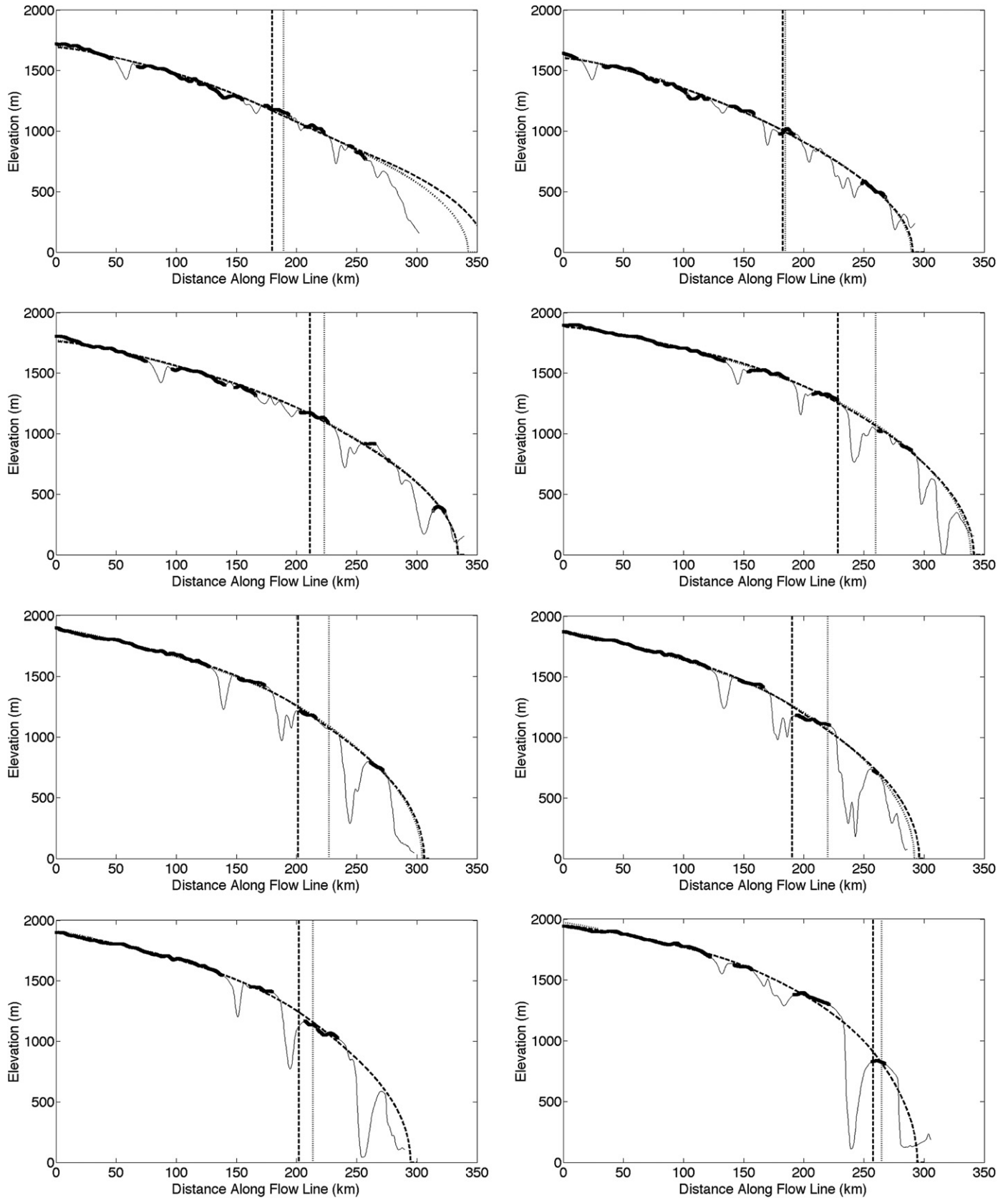


Fig. 8. Eight additional representative topographic profiles and model fits analogous to those in Figs. 6 and 7. (Left to right, and row by row starting at the top, the sequence of path numbers is 3, 12, 18, 26, 30, 31, 33, 39—cf. Fig. 3.) Fits using $n = 3$ are again denoted by dashed lines, and fits $n = 4$ are denoted by dotted lines. The quality of fits is very similar to that observed on the other 30 regular profiles that are not shown in this paper. In most cases, it is difficult to distinguish the fits visually on the scale plotted here—the primary differences are in the inferred positions of equilibrium lines.

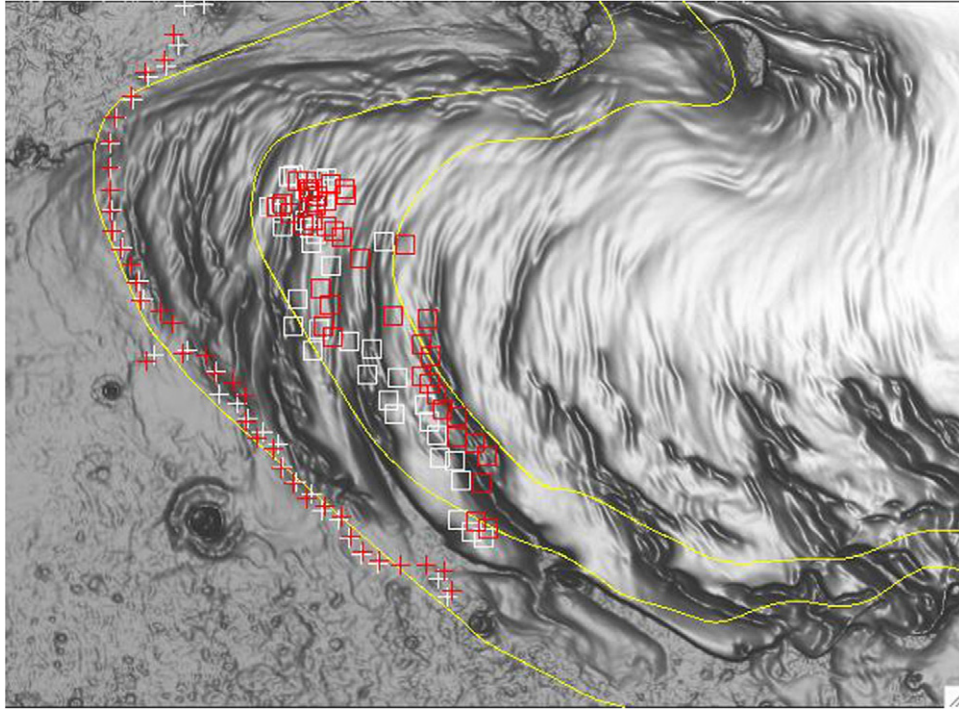


Fig. 9. Inferred locations of flow line termini (+ signs) and equilibrium line positions (squares) from model fits using $n = 3$ (red) and $n = 4$ (white). Elevation contours of the smoothed, interpolated surface at 20, 900 and 1300 m above Vastitas Borealis are shown in yellow. Inferred flow line terminus locations track the present-day edge of Titania Lobe as inferred from topography alone, except in Chasma Boreale, where inferred termini extend into the present-day chasma. The terminus locations for different flow-law exponents differ little, and so are difficult to distinguish when plotted on this scale. The inferred equilibrium line positions, however, are consistently lower for $n = 4$ than for $n = 3$. Inferred equilibrium line positions appear somewhat ‘noisy,’ consistent with the physically expected poorer resolving power for this parameter. They are not scattered wildly, however, but rather fall within a band of elevations 400 m wide, trending from higher in the east to lower in west.

we tested), but the decreases are slight (less than 2 m), and the corresponding model elevations differ from those obtained with $n = 6$ by no more than 1–2 m at any point (Fig. 10a). Such small differences may be at, or below, the limit of resolvability, given the ca. 1 m RMS vertical accuracy of MOLA (Smith et al., 2001a, 2001b, 2003) and the simplifications inherent in our model. [As an aside, estimates of equilibrium line locations are poorly determined in the large- n fits—see Fig. 10b—consistent with the facts that a surface profile undergoing plastic flow is independent of surface mass balance (Paterson, 1994) and that large- n flow laws approximate a plastic rheology.] Thus for this second group of flow lines, the high-fidelity fits with $n = 3$ –4 are accompanied by fits with $n = 6$ (and larger) which are almost indistinguishable from the former, and yet which systematically fit the data slightly more closely.

This hint of plastic flow around the tip of Titania Lobe could result from a systematic error in our assumed bed topography of just a few tens of meters on 100-km scales. It could also be an artifact of limited resolving power for n in our inverse method when applied to the particular inter-trough topography near the tip of the lobe. Alternatively, it could be real, in which case it would indicate a slight variation between material rheologies near the tip and the southern side of the lobe. We think that the question warrants further study. Our conclusion that all of the 40 flow lines are fit to high accuracy with values of $n = 3$ –4 is robust, however, in any case.

4. Interpretation

On Earth, nearly all ice caps flowing over frozen beds are shaped by a balance between flow and surface mass fluxes. Topographies of those caps are fit well by models similar to ours, whereas topographies of those (few) shaped by surface mass fluxes alone are not (Vialov, 1958; Paterson, 1969; Hutter, 1983). Fig. 11 shows examples of surface-elevation profiles from two terrestrial ice masses, together with the inter-trough topography from Fig. 6, after normalization to facilitate comparison.

The surface elevation profile of the East Antarctic Ice Sheet ranges from 3100 m at Vostok down to sea level at Mirny, over a horizontal distance of approximately 1120 km (Vialov, 1958). Assuming a flat bed at sea level, a surface accumulation rate of 0.5 cm of ice per year (Vialov, 1958), and a near-basal temperature of -6°C (Pattyn et al., 2004), we estimate a flow number $F = 1.1$ for this ice mass (cf. Appendix A.2). This accords with a large body of observations showing that the East Antarctic Ice Sheet is shaped by a balance between flow and surface mass fluxes. Indeed, the Vostok–Mirny profile can be fit well by a model similar to ours with the equilibrium line at the edge of the ice sheet (Vialov, 1958), which is appropriate because mass loss in East Antarctica occurs mainly by calving of icebergs into the surrounding ocean. We note also the qualitative similarity between the shape of the Vostok–Mirny transect and profile-shapes on Titania Lobe.

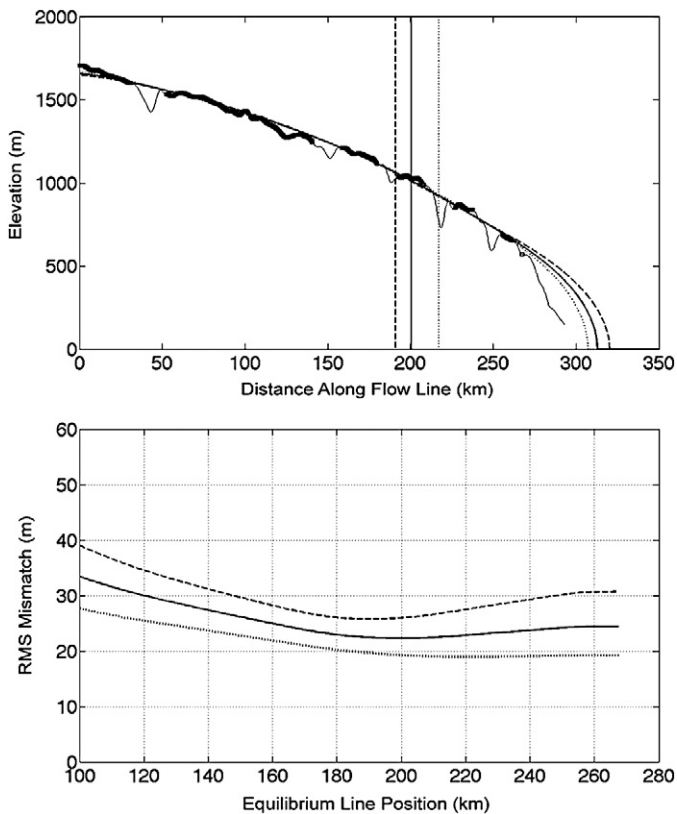


Fig. 10. (a) Representative data and model fits from path 4, on the tip of Titania Lobe, for flow law exponents $n = 3$ (dashed line, RMS difference between model and data of 25.9 m), $n = 4$ (solid line, 22.4 m RMS difference), and $n = 6$ (dotted line, 19.0 m RMS difference). (b) Plots of RMS differences for $n = 3$ (dashed line), $n = 4$ (solid line), and $n = 6$ (dotted line) vs equilibrium line position, as in Fig. 6b. Inferred positions of the equilibrium line differ little between fits with $n = 3$ and $n = 4$ in this case (and generally near the tip of the lobe, cf. Fig. 8), but the minima in RMS differences are broader than those for profiles on the southern side of the lobe. The minimum in RMS difference for $n = 6$ is very broad, suggesting that the profile is nearly independent of surface mass balance. Such independence would be consistent with a plastic flow law, in which n approaches infinity (Paterson, 1994).

By contrast, the shape of the Meighen Ice Cap in the Canadian Arctic differs qualitatively from any that we observe on Titania Lobe. The shape of Meighen Ice Cap is controlled by surface mass fluxes rather than by flow (Hutter, 1983). This is in accord with our estimate of $F = 0.01$ for this ice cap, based on dimensions reported by Paterson (1969), a surface ablation rate of 0.1 m per year (Koerner, 2005), and an assumed near-basal temperature of -5°C . It is also consistent with the inability of our ice-flow model to fit the Meighen thickness profile accurately—the slopes of all model profiles are largest near the terminus and decrease monotonically with increasing ice thickness toward the divide, whereas the slope of the Meighen thickness profile is maximum at intermediate thicknesses. Conversely, there is no known ice mass on Earth whose shape is dominated by surface mass fluxes but which mimics the shape of ice masses that are shaped by balance between flow and surface mass fluxes.

Likewise on Titania Lobe, we consider it implausible to postulate ad hoc variations of surface mass fluxes (in space and time) so as to yield current topography that mimics that shaped

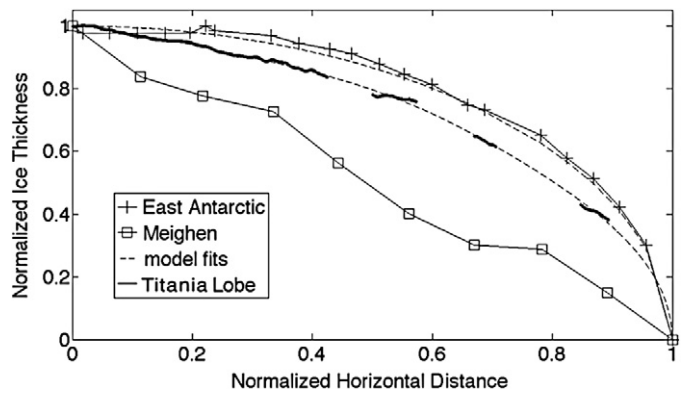


Fig. 11. Profiles of normalized ice thickness versus normalized horizontal distance for the Meighen Ice Cap in the Canadian Arctic (□), the East Antarctic Ice Sheet between Vostok and Mirny Stations (+), and Titania Lobe (specifically, the profile shown in Fig. 6, denoted by solid black lines). The normalization for ice thickness is the maximum ice thickness on the profile (for each profile separately). The normalization for horizontal distance is the length of the profile. The Meighen Ice Cap is the smallest of the three, with a maximum thickness of 85 m and extent of 2.5 km. The Vostok–Mirny traverse attains a thickness of 3100 m near Vostok and extends 1122 km. The data from Titania Lobe have been normalized by the thickness at the divide (1900 m) and extent of the flow line (320 km) inferred from the best fit of our ice-flow model to inter-trough topography using flow-law parameter $n = 3$ (using $n = 4$ yields a nearly identical plot). The dashed lines show the best fit model profile for $n = 3$ in the case of Titania Lobe, and the model of Vialov (1958) in the case of the East Antarctic data.

by balance between flow and surface fluxes—and moreover does so only for topography *between* troughs. We therefore know of no physical mechanism other than flow that could produce the inter-trough topography on Titania Lobe so consistently. We interpret the consistency and fidelity of fits on widely separated profiles as evidence that our ice-flow model captures the essential physics responsible for the topography.

Our interpretation requires, however, that the troughs were occupied by flowing ice at the time that the inter-trough topography formed. We infer that the troughs must post-date the inter-trough topography, which in turn requires a significant change in the distribution, and perhaps magnitude, of surface mass balances on Titania Lobe.

The ice-flow model fits inter-trough topography closely over nearly the full range of elevation (cf. Figs. 6, 8, 10, and 11). This indicates that troughs have incised the prior surface so rapidly, compared to the time-scale of ice flow during trough formation, that the record preserved in the inter-trough topography remained nearly undisturbed. Neither has flow subsequent to trough formation had sufficient time to deform inter-trough topography very much, either because flow has been slow, or time has been short, or both.

5. Conclusions

We have presented strong evidence that ice flow has shaped the topography of the NPLD, at least on Titania Lobe, during some time in the past. We derive the evidence for flow from inter-trough topography that (we infer) survives from a previous era. Inspection of Fig. 1b suggests that much less ‘relict’

topography survives elsewhere on the NPLD, and thus that Titania Lobe may have been glaciologically active more recently than other regions of the NPLD, or that ‘relict’ topography has been better preserved there. Either of these conclusions, if confirmed, would have broad and significant implications for where to seek, and how to analyze, martian climate records preserved in the NPLD. We therefore regard not merely strong, but conclusive tests of our scenario to be a priority for our future work.

Recent and continuing observations of internal stratigraphy in the NPLD using radar (Picardi et al., 2005; Phillips et al., 2007; Holt et al., 2007) will allow conclusive tests of our scenario. In particular, internal layers in our scenario must intersect the (inter-trough) surface of the ice at all elevations in the inferred ablation zone, whereas layers in the accumulation zone can never intersect the ice surface (Fisher, 2000; Siegert and Fisher, 2002; Koutnik et al., 2006).

If our scenario survives conclusive testing, a key question would clearly be *when* the inferred change in the mass balance regime occurred. Because our model fits imply no absolute time scale, we cannot yet constrain the timing of the change in mass balance regime or the age of the inter-trough surface. The path toward such constraint is clear, however, and it again involves radar stratigraphic observations. During the postulated era of flow, internal layers shaped by deposition and flow would have extended unbroken across spaces now occupied by troughs. Later alteration of the surface by trough formation must have resulted in new stresses that strained ice, and so deformed layers, in the vicinity of trough walls. The spatial extent and shape of layer deformation would depend on the surface temperature history and time over which the new stresses have acted. Thus radar observations of layering near troughs, in combination with flow modeling under current and recently past temperature-conditions (cf. Pathare and Paige, 2005), may yield an upper bound on the time since the onset of trough formation.

Finally, the time-scales of variations in martian climate (whether due to obliquity or other variations) imply limits on the time available to establish a (near-)steady-state topography during the past era of flow. Those limits can be linked, via a transient analysis based on our flow model, to lower limits on flow speeds, and thus on temperatures, near the base of Titania Lobe (Koutnik et al., 2007; cf. also Appendix A). Such temperature information would have implications for temperatures over a wide area on Vastitas Borealis and, in combination with timing information, could yield significant new insight into recent martian climate history.

Acknowledgments

We thank I.R. Joughin for helpful conversations on flow-line delineation and for providing to us his gradient-finding routine. This work was supported by NASA grant NNX06AD99G and NSF grant OPP 0440666.

Appendix A

A.1. Selection of surface-elevation data

Here we detail our delineation of inter-trough topography and construction of flow paths and bands during the postulated era of ice flow, prior to formation of the present-day troughs (at which time the spaces currently occupied by troughs would have contained flowing ice).

As discussed in Section 2.1, exclusion of parts of the surface where the slope exceeds a low threshold (0.015 rad) yields a surface that largely corresponds to the inter-trough topography we would infer from inspection of the MOLA DEM. Thin, curvilinear strips of topography near the bottoms of trough remain after thresholding, however, because slopes along the bottoms of the troughs are generally small—those orthogonal to the local axis of a trough are near the point where they change sign, and slopes along the axis are typically small. To remove such strips from our estimate of inter-trough topography, we perform a two-step operation. First, we smooth the thresholded, fragmentary surface by averaging on the scale of trough widths (pixel-locations where thresholding has excluded data are assigned the value not-a-number, i.e., NaN). Empirically, we find the scale of trough widths to be approximately 40 km. We then exclude DEM pixels on the thresholded surface whose elevations differ from corresponding pixels on the smoothed surface by more than 200 m, which we find, again empirically, to reliably exclude nearly all trough bottoms. The remaining thresholded (low-slope) MOLA data constitute our estimate of inter-trough topography as shown in Fig. 3.

Next we construct a surface from which to estimate flow paths and corresponding flow bands around each path. We use Delauney triangulation on the inter-trough topography to form an interpolation grid in locations occupied by troughs. We then interpolate linearly across gaps in the inter-trough topography and smooth the result on scales up to that of typical trough widths (again, roughly 40 km).

We use a gradient-finding routine, seeded at points on the -4900 m elevation contour, to find pixel locations both down- and up-hill along prospective flow paths and flow-band edges. The latter are merely flow paths seeded near the central path on either side. The flow band width at a given point on the flow line is the length of a line segment through that point, orthogonal to the flow-line direction, and with its endpoints on the flow band-boundaries. We estimate the local flow line direction by fitting a line to points near the point in question. We computed flow bands around the lines in Fig. 4 with typical widths of about 6 km wide at elevations near the planum (which we observed to limit elevation variations across the flow band to about 25 m). For regular paths, widths decrease almost monotonically as the flow lines climb onto the apparent ice divide. Empirically, width estimates become numerically unreliable for estimates less than one-tenth of the DEM pixel spacing, i.e., 11.5 m for the DEM used here. We therefore terminate flow bands (i.e., taper them rapidly to zero-width) at the point where their widths decrease to that value.

Our final step in data selection is to extract actual MOLA elevations along the flow lines where those lines traverse inter-trough topography (*not* elevations on the surface used to derive the flow lines). Together with the flow band widths, these data are the input to our inverse problem.

A.2. Characterizing flow regimes in ice masses

An ice mass can fall into one of three distinct regimes. In a stagnant regime, surface mass exchange alone controls surface topography. In a near-equilibrium regime, both surface mass exchange and flow control surface shape. In a surging regime, ice flow alone controls surface elevation change. Here, we use characteristic values of accumulation rate, temperature, and ice-mass shape to derive a single, nondimensional flow number, F , which identifies which regime is in effect for any ice mass frozen to its bed.

Consider first a three-dimensional ice mass that does not vary in time. In such an ice mass, ice flows along paths from an ice divide to the ice-sheet margin, where (by definition) the ice thickness decreases to zero. Along a given flow path, the path length x ranges from 0 at the divide to L at the margin. We take z as the vertical coordinate. The ice-flow velocity components in directions x and z are u and w , respectively. The ice thickness, $h(x)$, ranges from $h(0) = H$ at the divide to $h(L) = 0$ at the margin. Flow paths tend to follow surface gradients, so they are generally curvilinear (projected onto the plane of the bed). Commonly, however, closely spaced flow paths differ only slightly in direction at any point along their length. A pair of such flow paths, separated by distance $W(x)$ [along with the surface and bed elevations $S(x)$ and $B(x)$] define a volume of ice with zero flow across the bounding lateral flow paths, i.e., a flow band. We choose flow bands defined by pairs of narrowly separated flow paths, such that the horizontal velocity $u(x, z, t)$ can be taken to be uniform across the flow band. (In practice, the velocity field is unknown a priori, so we choose pairs of flow paths such that the change in ice thickness across the width of the flow band is small compared to the thickness at the center of the band, for each x —cf. Appendix A.1.) In this case, we say the width, $W(x)$ is ‘small,’ and ice flow can be well-approximated using a 2-dimensional ice-flow model in place of a full, 3-dimensional model.

Now suppose the ice mass is allowed to vary in time, though in such a way that flow paths and flow band widths remain constant in time (i.e., perturbatively). Let the net surface mass-balance rate (units of ice volume area⁻¹ time⁻¹) along the flow line be $\dot{b}(x, t)$, where $\dot{b}(x, t) > 0$ denotes a net accumulation rate and $\dot{b}(x, t) < 0$ denotes a net ablation rate. For martian PLD, we assume that there is no vertical mass flux at the base of the ice (i.e., no melting or freezing).

When $W(x)$ is small as defined above, the dynamic flux of ice through any cross-section across the flow band can be written as

$$q_d(x, t) = h(x, t)W(x)\bar{u}(x, t), \quad (\text{A.1})$$

where $h(x, t)$ is the time-dependent ice thickness at location x , and $\bar{u}(x, t)$ is the vertical average of the horizontal-velocity component $u(x, z, t)$. This velocity $\bar{u}(x, t)$ depends on the rheological properties of the ice, and on the stress to which it is subjected.

The shear stress τ_{xz} acting horizontally on horizontal planes in the ice at depth $S - z$, is given by

$$\tau_{xz}(x, z, t) = -\rho g[S(x, t) - z] \frac{\partial S(x, t)}{\partial x}, \quad (\text{A.2})$$

where ρ is the ice density (taken to be constant over depth and x), g is the acceleration due to gravity on Mars, and $\partial S/\partial x$ is the surface slope at x . When ice thickness, slope, and velocity vary slowly on length scales much larger than the ice thickness, this shear stress is much more important than longitudinal stresses, and $\partial u/\partial z$ is much larger than other velocity gradients. In the shallow-ice approximation (SIA) (e.g., Paterson, 1994, p. 262), longitudinal stresses and these other velocity gradients are neglected. Experiments show that shear stress τ_{xz} is related to shear strain rate $\dot{\epsilon}_{xz} = 1/2(\partial u/\partial z + \partial w/\partial x)$, by a flow law of the form (Glen, 1955; Goldsby and Kohlstedt, 2001)

$$\dot{\epsilon}_{xz} = A(\theta)\tau_{\text{eff}}^{n-1}\tau_{xz}, \quad (\text{A.3})$$

where θ is (absolute) temperature, $A(\theta)$ is a temperature-dependent pre-factor, τ_{eff} is the second invariant of the deviatoric stress tensor (Paterson, 1994, p. 91), and n is the flow-law exponent. In the SIA, this reduces to

$$\dot{\epsilon}_{xz} = \frac{1}{2} \frac{\partial u}{\partial z} = A(\theta)\tau_{xz}^n. \quad (\text{A.4})$$

The pre-factor, $A(\theta)$, depends on temperature through an Arrhenius relation,

$$A(\theta) = A_0 \exp\left(\frac{Q}{k_B N_A \theta}\right), \quad (\text{A.5})$$

where A_0 depends on the deformation mechanisms at the crystal scale (and thus on ice characteristics such as grain size) but not on temperature, Q is the activation energy for the mechanism(s), k_B is Boltzmann constant, and N_A is Avogadro number. We assume that $A(\theta)$ does not vary with depth or between flow lines, which is effectively an assumption that the temperature of basal ice, where most of the strain occurs, is uniform over our model domain.

When the ice is everywhere frozen to its bed, the horizontal velocity $u(x, B(x))$ is zero at $z = B(x)$, and Eq. (A.4) can be integrated from the bed to give

$$u(x, z, t) = \frac{2A(\theta)}{(n+1)} (\rho g)^n h^{n+1} \left| \frac{\partial S}{\partial x} \right|^{n-1} \times \left(-\frac{\partial S}{\partial x} \right) \left(1 - \left[1 - \frac{z - B(x)}{h} \right]^{n+1} \right). \quad (\text{A.6})$$

A second vertical integration (Paterson, 1994, Chap. 11, Eqs. 20–22) gives the depth-averaged velocity

$$\bar{u}(x, t) = \frac{2A(\theta)}{n+2} (\rho g)^n h^{n+1} \left| \frac{\partial S}{\partial x} \right|^{n-1} \left(-\frac{\partial S}{\partial x} \right). \quad (\text{A.7})$$

Letting over-dots represent rates of change, or partial derivatives with respect to time, conservation of mass allows us to write an evolution equation for ice surface $S(x, t)$,

$$W(x)\dot{S}(x, t) = W(x)\dot{b}(x, t) - \frac{\partial q_d(x, t)}{\partial x}. \quad (\text{A.8})$$

Equation (A.8) shows that surface evolution \dot{S} is driven by either mass exchange \dot{b} at the surface, or by flow divergence $\partial q_d/\partial x$, or by both.

Writing $q_d(x, t)$ in terms of ice-mass thickness, slope, and temperature using Eq. (A.7),

$$W(x)\dot{S}(x, t) = W(x)\dot{b}(x, t) - \frac{\partial}{\partial x} \left[W(x) \frac{2A(\theta)}{n+2} (\rho g H_0)^n h^{n+2} \times \left| \frac{\partial S}{\partial x} \right|^{n-1} \left(-\frac{\partial S}{\partial x} \right) \right]. \quad (\text{A.9})$$

In order to understand the order of magnitude of the various terms, we nondimensionalize Eq. (A.9), using characteristic values H_0 , L_0 , W_0 , and \dot{b}_0 , for ice thickness, flow-band length, width, and surface mass-balance rate, respectively. Letting tildes indicate nondimensional variables of order unity,

$$\begin{aligned} \tilde{x} &= x/L_0, & \tilde{t} &= t/(H_0/\dot{b}_0), \\ \tilde{b}(\tilde{x}, \tilde{t}) &= \dot{b}(x, t)/\dot{b}_0, & \tilde{h}(\tilde{x}, \tilde{t}) &= h(x, t)/H_0, \\ \tilde{S}(\tilde{x}, \tilde{t}) &= S(x, t)/H_0, & \tilde{W}(\tilde{x}) &= W(x)/W_0. \end{aligned} \quad (\text{A.10})$$

Substituting the expressions in Eq. (A.10) into Eq. (A.9) yields a dimensionless continuity equation,

$$\begin{aligned} \tilde{S}(\tilde{x}, \tilde{t}) - \tilde{b}(\tilde{x}, \tilde{t}) \\ = -F \frac{1}{\tilde{W}(\tilde{x})} \frac{\partial}{\partial \tilde{x}} \left[\tilde{W}(\tilde{x}) [\tilde{h}(\tilde{x}, \tilde{t})]^{n+2} \left| \frac{\partial \tilde{S}(\tilde{x}, \tilde{t})}{\partial \tilde{x}} \right|^{n-1} \right. \\ \left. \times \left(-\frac{\partial \tilde{S}(\tilde{x}, \tilde{t})}{\partial \tilde{x}} \right) \right], \end{aligned} \quad (\text{A.11})$$

where the nondimensional variables \tilde{b} , \tilde{W} , and \tilde{h} are all $O(1)$ by construction. With the additional assumption that any trend in bed elevation $B(x)$ is much smaller than the trend in the ice surface elevation $S(x)$, the surface slope $\partial \tilde{S}/\partial \tilde{x}$ and the flux divergence $\partial/\partial \tilde{x} [(1/\tilde{W})(\tilde{h})^{n+2}(\partial \tilde{S}/\partial \tilde{x})^n]$ are also $O(1)$. All units and orders of magnitude are absorbed by the nondimensional constant F , which we call the flow number, given by

$$F = \left[\frac{2A(\theta)}{n+2} (\rho g H_0)^n \left(\frac{H_0}{L_0} \right)^{n+1} \left(\frac{H_0}{\dot{b}_0} \right) \right]. \quad (\text{A.12})$$

First we recognize that $\mathcal{T}_b = H_0/\dot{b}_0$ is a characteristic time for surface mass exchange, i.e., the time to build a stagnant ice mass to characteristic thickness H_0 at the characteristic accumulation rate \dot{b}_0 . Second, we recognize that a characteristic flow speed u_0 can be defined by using (H_0/L_0) as a characteristic surface slope, and inserting characteristic numbers into Eq. (A.7) to get

$$u_0 = \frac{2A(\theta)}{n+2} \left(\rho g \frac{H_0}{L_0} \right)^n H_0^{n+1}. \quad (\text{A.13})$$

This characteristic flow speed can be used to form a characteristic flow time

$$\mathcal{T}_u = \frac{L_0}{u_0} = \left[\frac{2A(\theta)}{n+2} (\rho g H_0)^n \left(\frac{H_0}{L_0} \right)^{n+1} \right]^{-1} \quad (\text{A.14})$$

which is the time for ice to move the length L_0 of the flow band at speed u_0 . Now the nondimensional number F can be written as the ratio of these two characteristic times,

$$F = \frac{\mathcal{T}_b}{\mathcal{T}_u}. \quad (\text{A.15})$$

Now we can characterize the three regimes of flow in terms of flow number F . First, if $F \ll 1$, the right side of Eq. (A.11) is negligibly small because all other factors are $O(1)$. Equation (A.11) reduces to

$$\tilde{S}(\tilde{x}, \tilde{t}) - \tilde{b}(\tilde{x}, \tilde{t}) = 0 \quad (\text{A.16})$$

which shows that mass exchange \tilde{b} at the surface is the only process shaping the surface topography, i.e., the ice mass is stagnant.

Second, if F is $O(1)$, then both the surface-exchange term on the left and the flow-divergence term on the right in Eq. (A.11) are $O(1)$. The surface-evolution term \tilde{S} then must also be $O(1)$, or smaller if the other two terms tend to cancel each other, creating a steady state of flow. This equilibrium or near-equilibrium between surface mass exchange and flow is the regime in which most terrestrial glaciers and ice sheets are found.

Finally, if $F \gg 1$, then the flow-divergence term on the right in Eq. (A.11) is very large. In order to balance the equation, the surface-evolution term \tilde{S} on the left side must also be very large, because \tilde{b} is only $O(1)$. As a result, surface mass exchange \tilde{b} is negligible by comparison to flow divergence,

$$\begin{aligned} \tilde{S}(\tilde{x}, \tilde{t}) = -F \frac{1}{\tilde{W}(\tilde{x})} \frac{\partial}{\partial \tilde{x}} \left[\tilde{W}(\tilde{x}) [\tilde{h}(\tilde{x}, \tilde{t})]^{n+2} \left| \frac{\partial \tilde{S}(\tilde{x}, \tilde{t})}{\partial \tilde{x}} \right|^{n-1} \right. \\ \left. \times \left(-\frac{\partial \tilde{S}(\tilde{x}, \tilde{t})}{\partial \tilde{x}} \right) \right], \end{aligned} \quad (\text{A.17})$$

and the surface evolves entirely in response to flow (Nye, 2000). This regime also operates in surging terrestrial glaciers (e.g., Kamb et al., 1985), although in those glaciers, the fast flow is due to fast basal sliding, a process not explicitly included in our analysis here.

A.3. Surface-elevation modeling based on steady-state ice flow

The ice-flow model in our inverse problem applies in the case where F is $O(1)$, i.e., where mass balance and flow are in equilibrium (or nearly so) and together control the surface-elevation profile. Here we derive the ice-flow model and display the resulting equation for the surface-elevation profile.

We now assume that the bed $B(x)$ is flat, and is situated at level $z = 0$, so that $S(x, t) = h(x, t)$. To represent a steady state, we set $\dot{S}(x, t) = 0$ in Eq. (A.8). By integrating Eq. (A.8) from the ice divide at $x = 0$ to a position x , we find the kinematic

flux $q_k(x)$,

$$q_k(x) = \int_0^x \dot{b}(x') W(x') dx', \quad (\text{A.18})$$

which is the net ice volume that must move through the cross-section of the flow band at x in unit time. The dynamic flux $q_d(x)$ (no longer a function of time) is given by Eq. (A.1) with the depth-averaged velocity $\bar{u}(x)$ given by Eq. (A.7). For equilibrium (i.e., steady-state), the dynamic flux must transport exactly the kinematic flux. Equating $q_k(x)$ and $q_d(x)$ gives

$$q_k(x) = \left[\frac{2A(\theta)}{n+2} \right] (\rho g)^n W(x) [h(x)]^{n+2} \left| \frac{dh}{dx} \right|^{n-1} \left(-\frac{dh}{dx} \right), \quad (\text{A.19})$$

where $A(\theta)$ is the only factor that depends on temperature.

Equation (A.19) is a first-order differential equation for $h(x)$ which can be solved simply by quadrature. Integration using the terminus as the lower limit yields

$$\frac{1}{\rho g} \left[\frac{n+2}{2A(\theta)} \right]^{\frac{1}{n}} \int_x^L \left[\frac{q_k(x')}{W(x')} \right]^{\frac{1}{n}} dx' = \frac{n}{2n+2} [h(x)]^{2+\frac{2}{n}}. \quad (\text{A.20})$$

Using the fact $h(x) = H$ at $x = 0$, Eq. (A.20) can be nondimensionalized by dividing both sides by the corresponding expressions at $x = 0$:

$$\frac{1}{\beta} \int_x^L \left[\frac{q_k(x')}{W(x')} \right]^{\frac{1}{n}} dx' = \left[\frac{h(x)}{H} \right]^{2+\frac{2}{n}}, \quad (\text{A.21})$$

where β is a constant on a given flow line and is determined by the flow-band geometry and mass-balance distribution:

$$\beta = \int_0^L \left[\frac{q_k(x')}{W(x')} \right]^{\frac{1}{n}} dx'. \quad (\text{A.22})$$

Note that the temperature-dependence of the ice flow law has canceled out of Eq. (A.21), as has any scalar factor multiplying the accumulation-rate pattern $\dot{b}(x)$ in $q_k(x)$.

Our model for the steady-state mass-balance distribution is

$$\dot{b}(x) = \begin{cases} c, & 0 \leq x < R, \\ -a, & R \leq x \leq L, \end{cases} \quad (\text{A.23})$$

where $c > 0$ is the accumulation rate, $a > 0$ is the ablation rate, and R is the position of the equilibrium line. The steady-state condition requires that

$$1 + \frac{c}{a} = \frac{\int_0^L W(x') dx'}{\int_0^R W(x') dx'}. \quad (\text{A.24})$$

Using this particular mass-balance distribution in Eq. (A.18), the kinematic flux through the flow-band cross section at x is

$$q_k(x) = a \begin{cases} \frac{c}{a} \int_0^x W(x') dx', & 0 \leq x < R, \\ \frac{c}{a} \int_0^R W(x') dx' - \int_R^x W(x') dx', & R \leq x \leq L. \end{cases} \quad (\text{A.25})$$

From Eqs. (A.21), (A.22), and (A.25), it is clear that both β and the integral it multiplies in Eq. (A.21) are proportional to $a^{\frac{1}{n}}$. Thus the absolute ablation rate also cancels out of Eq. (A.21), leaving our model dependent only on the ratio of accumulation and ablation rates, or equivalently on the equilibrium line position [cf. Eq. (A.24)]. Together with the cancellation of $A(\theta)$, this leaves no information in the model on absolute flow or mass flux rates—the computed surface elevations can equally well result from small surface mass fluxes and slow flow, or from large fluxes and fast flow.

We fit the model surface given by Eq. (A.21), with $q_k(x)$ given by Eq. (A.25), to inter-trough topography by varying H , L , R , and n .

The solution of Paterson (1994, Chap. 11, Eqs. 12 and 13) can be recovered exactly from ours by setting $W(x)$ equal to any finite constant for all x .

References

- Bamber, J.L., 2004. Modeling ice sheet dynamics with the aid of satellite-derived topography. In: Kelly, R.J., Drake, N., Barr, S. (Eds.), *Spatial Modeling of the Terrestrial Environment*. John Wiley, New York, pp. 13–34.
- Budd, W.F., Jenssen, D., Leach, J.H.I., Smith, I.N., Radok, U., 1986. The north polar ice cap of Mars as a steady-state system. *Polarforschung* 56, 46–63.
- Cutts, J.A., 1973. Nature and origin of layered deposits of the martian polar regions. *J. Geophys. Res.* 78, 4231–4249.
- Ekholm, S., Keller, K., Bamber, J.L., Gogineni, S.P., 1998. Unusual surface morphology from digital elevation models of the Greenland ice sheet. *Geophys. Res. Lett.* 25, 3623–3626.
- Fishbaugh, K.E., Hvidberg, C.S., 2006. Martian north polar layered deposits stratigraphy: Implications for accumulation rates and flow. *J. Geophys. Res.* 111, doi:10.1029/2005JE002571.
- Fisher, D.A., 1993. If martian ice caps flow: Ablation mechanisms and appearance. *Icarus* 105, 501–511.
- Fisher, D.A., 2000. Internal layers in an “accublation” ice cap: A test for flow. *Icarus* 144, 289–294.
- Fisher, D.A., Winebrenner, D.P., Stern, H., 2002. Lineations on the “white” accumulation areas of the residual northern ice cap of Mars: Their relation to the “accublation” and ice flow hypothesis. *Icarus* 159, 39–52.
- Glen, J.W., 1955. The creep of polycrystalline ice. *Proc. R. Soc. London A* 228 (1175), 519–538.
- Goldsby, D.L., Kohlstedt, D.L., 2001. Superplastic deformation of ice: Experimental observations. *J. Geophys. Res.* 106 (B6), 11017–11030.
- Greve, R., Mahajan, R., 2005. Influence of ice rheology and dust content on the dynamics of the north polar cap of Mars. *Icarus* 174, 475–485.
- Greve, R., Mahajan, R.A., Segschneider, J., Grieger, B., 2004. Evolution of the north-polar cap of Mars: A modeling study. *Planet. Space Sci.* 52, 775–787.
- Herkenhoff, K., Plaut, J.J., 2000. Surface ages and resurfacing rates of the polar layered deposits on Mars. *Icarus* 144, 243–255.
- Holt, J.W., and 15 colleagues, 2007. Initial SHARAD observations of internal layers in the uppermost north pole layered deposits of Mars. In: 7th International Conference on Mars. Abstract 3372.
- Howard, A.D., Cutts, J.A., Blasius, K.R., 1982. Stratigraphic relationships with martian polar cap deposits. *Icarus* 50, 161–215.
- Hutter, K., 1983. *Theoretical Glaciology*. D. Reidel Publishing, Tokyo.
- Hvidberg, C.S., 2003. Relationship between topography and flow in the north polar cap on Mars. *Ann. Glaciol.* 37, 363–369.
- Ivanov, A., Muhleman, D.O., 2000. The role of sublimation for the formation of the northern ice cap: Results from the Mars Orbiter Laser Altimeter. *Icarus* 144, 436–448.
- Kamb, B., Raymond, C.F., Harrison, W.D., Engelhardt, H., Echelmeyer, K.A., Humphrey, N., Brugman, M.M., Pfeffer, T., 1985. Glacier surge mechanism: 1982–1983 surge of Variegated Glacier, Alaska. *Science* 227, 469–479.

- Koerner, R.M., 2005. Mass balance of glaciers in the Queen Elizabeth Islands, Nunavut, Canada. *Ann. Glaciol.* 42 (1), 417–423.
- Koutnik, M., Waddington, E., Winebrenner, D., 2006. Inferring spatial patterns of accumulation from radar internal layers. In: Fourth International Conference on Mars Polar Science and Exploration. Abstract 8036.
- Koutnik, M.R., Waddington, E.D., Neumann, T.A., Winebrenner, D.P., 2007. Response time-scales for martian ice masses. In: 7th International Conference on Mars. Abstract 3189.
- Laskar, J., Levrard, B., Mustard, J., 2002. Orbital forcing of the martian polar layered deposits. *Nature* 419, 375–377.
- Levrard, B., Forget, F., Montmessin, F., Laskar, J., 2007. Recent formation and evolution of northern martian polar layered deposits as inferred from a Global Climate Model. *J. Geophys. Res.* 112, doi:10.1029/2006JE002772. E06012.
- Nye, J.F., 2000. A flow model for the polar caps of Mars. *J. Glaciol.* 46 (154), 438–444.
- Paterson, W.S.B., 1969. The Meighen ice cap, Arctic Canada: Accumulation, ablation and flow. *J. Glaciol.* 8 (51), 341–352.
- Paterson, W.S.B., 1972. Laurentide ice sheet: Estimated volumes during late Wisconsin. *Rev. Geophys. Space Phys.* 10, 885–917.
- Paterson, W.S.B., 1994. *The Physics of Glaciers*, fourth ed. Pergamon, Oxford.
- Pathare, A.V., Paige, D.A., 2005. The effects of martian orbital variations upon the sublimation and relaxation of north polar troughs and scarps. *Icarus* 174, 419–443.
- Pattyn, F., De Smet, B., Souchez, R., 2004. Influence of subglacial Vostok lake on the regional ice dynamics of the Antarctic ice sheet: A model study. *J. Glaciol.* 50 (171), 583–589.
- Pettit, E.C., Waddington, E.D., 2003. Ice flow at low deviatoric stress. *J. Glaciol.* 49 (166), 359–369.
- Phillips, R.J., and 17 colleagues, 2007. Stratigraphy of the north polar deposits as mapped by sounding radars. In: 7th International Conference on Mars, Abstract 3042.
- Picardi, G., and 33 colleagues, 2005. Radar soundings of the subsurface of Mars. *Science* 310, 1925–1928.
- Siegert, M.J., Fisher, D.A., 2002. A terrestrial analogy for martian accretion zones revealed by airborne ice-penetrating radar from the East Antarctic ice sheet. *Icarus* 157, 264–267.
- Smith, D.E., and 23 colleagues, 2001a. Mars Orbiter Laser Altimeter: Experiment summary after the first year of global mapping of Mars. *J. Geophys. Res.* 106 (E10), 23689–23722.
- Smith, D.E., Zuber, M.T., Neumann, G.A., 2001b. Seasonal variations of snow depth on Mars. *Science* 294, 2141–2146.
- Smith, D., Neumann, G., Arvidson, R.E., Guinness, E.A., Slavney, S., 2003. Mars Global Surveyor Laser Altimeter Mission Experiment Gridded Data Record. NASA Planetary Data System, MGS-M-MOLA-5-MEGDR-L3-V1.0.
- Thomas, P., Squyres, S., Herkenhoff, K., Howard, A., Murray, B., 1992. Polar deposits of Mars. In: Kieffer, H.H., Jakosky, B.M., Snyder, C.W., Matthews, M.S. (Eds.), *Mars*. University of Arizona Press, Tucson, AZ, pp. 767–795.
- Touma, J., Wisdom, J., 1993. The chaotic obliquity of Mars. *Science* 259, 1294–1297.
- Vialov, S.S., 1958. Regularities of glacial shield movements and the theory of plastic viscous flow. *J. Int. Assoc. Sci. Hydrol.* 47, 266–275.
- Waddington, E.D., Neumann, T.A., Koutnik, M.R., Marshall, H.-P., Morse, D.L., 2007. Inference of accumulation-rate patterns from deep radar layers in glaciers and ice sheets. *J. Glaciol.* 53 (183), 694–712.
- Zuber, M.T., and 20 colleagues, 1998. Observations of the north polar region of Mars from the Mars Orbiter Laser Altimeter. *Science* 282 (5396), 2053–2060.
- Zwally, H.J., Fountain, A., Kargel, J., Kouvaris, L., Lewis, K., MacAyeal, D., Pfeffer, T., Saba, J.L., 2000. Morphology of Mars north polar ice cap. In: 2nd International Conference on Mars Polar Science and Exploration. Abstract 1057.